Hybrid Microchannel Heat Sink with Sustainable Cooling Solutions: Numerical Model Validation

Wan Mohd. Arif Aziz Japar[1,*], Nor Azwadi Che Sidik[1], R. Saidur[2], Natrah Kamaruzaman[3], Yutaka Asako[1], Siti Nurul Akmal Yusof[4], Mohd Nizam Lani[5]

[1] Malaysian-Japan International Institute of Technology, Universiti Teknologi Malaysia, 54100 Kuala Lumpur, Wilayah Persekutuan Kuala Lumpur, Malaysia
[2] Research Centre for Nano-Materials and Energy Technology, School of Science and Technology, Sunway University, Bandar Sunway, 47500 Subang Jaya, Selangor, Malaysia
[3] Department of Thermofluid, School of Mechanical Engineering, Faculty of Engineering, Universiti Teknologi Malaysia, 81310 Skudai, Johor, Malaysia
[4] Faculty of Innovative Design and Technology, Universiti Sultan Zainal Abidin, Kampus Gong Badak, 21300 Kuala Nerus, Terengganu Darul Iman, Malaysia
[5] Faculty of Fisheries and Food Science, Universiti Malaysia Terengganu, 21030, Kuala Nerus, Terengganu, Malaysia

ARTICLE INFO	ABSTRACT
	Miniaturization and utilization of low-dimensional structures of recent electronic devices have witnessed some new micro cooling methods which can fulfil the cooling demand for the electronic devices. Microchannel heat sink (MCHS) is one of the micro cooling method which appears as a promising method that can provide high heat transfer rate due to small hydraulic diameter. Furthermore, microchannel heat sink is easy to be fabricated compare to other micro cooling device. Due to fast development in electronic industry, hybrid microchannel heat sink with optimal design has received a great deal of attention in order to provide sustainable cooling solutions. However, most of the studies of hybrid microchannel heat sink only provided the numerical analysis without any validation of the proposed design experimentally. This is very important since it also will determine whether the proposed hybrid microchannel heat sink can be fabricated or not. Therefore, the aim of this article is to validate the numerical model of hybrid microchannel heat sink (TC-RR-SC MCHS) experimentally. The validation result showed that the maximum discrepancy between both simulation and experimental analyses for Nusselt number and friction factor were 15.8% and 17.4%, respectively, which is less than 20%. The different number of microchannels between the simulated TC-RR-SC MCHS and fabricated TC-RR-SC MCHS is one of the factors that contribute to the data discrepancy. Furthermore, the poor finishing during the fabrication process also another factor because the burrs and debris at the top and bottom surface of microchannels affect the convective heat transfer area and the flow area of fluid.

1. Introduction

Application of cooling system in thermal engineering is recognised and have been studied both theoretically and practically in building energy system, electronic devices, chemical vapour deposition instruments, solar energy collectors, furnace engineering and many more [1]. In recent years, thermal management of electronic devices is of interest as a new generation of high performing dense chip packages that function at high frequency produces a very high heat flux on the electronic devices. Prolonged heat flux creates a hot spot on the electronic devices and reduces the lifespan of the electronic devices due to the acceleration of the Mean Time to Failure (*MTTF*) as described by the Black's equation [2]. Thermal management of compact electronic devices that operate at high power density is critical as there is a lack of efficient technique to remove heat dissipation from the electronic devices [3]. The increase in power density and miniaturisation of electronic packages has changed the direction of cooling system technology, from air-cooling technology to advanced heat transfer technology due to the inadequacy of conventional method to remove extreme high heat flux [4].

Several methods have been proposed in the previous studies to improve the cooling performance, such as air cooling method [5], heat pipe method [6], use of liquid material as a coolant [7], and micro-cooling method [8]. Micro-cooling is a good technique due to its high cooling efficiency compared to the other methods. Even though the air cooling method is the simplest cooling technique, it has a low cooling efficiency with additional heat generation by the fan itself [9]. Meanwhile, for the liquid material and heat pipe applications, space is required to accommodate additional system for condensation process [9] which are not suitable for compact electronic devices. Therefore, the micro-cooling method is one of the promising techniques that can dissipate a very high heat flux generated by the compact electronic devices that can be attributed to the high heat transfer surface-area-to-volume ratio. Besides that, the micro hydraulic diameter also contributes to the heat transfer performance enhancement due to the augmentation of heat transfer coefficient [10]. When the micro-cooling method was used, microchannel heat sink (MCHS) was found to be the most prospective as a very high heat flux can be removed compared to micro-jet impingement, micro-heat pipe and micro-electro-hydrodynamic methods [11]. In 1981, Tuckerman and Pease [12] reported that rectangular MCHS can remove heat-flux up to 790 W/cm^2. However, the pumping power required by the MCHS was very high due to high-pressure drop penalty generated in the microchannel. Based on the study of Japar *et al.,* [13], high-pressure drop penalty was attributed to high wall shear stress in the developing region of laminar flow. The discovery motivated many scholars to develop hybrid MCHS that integrated by more than one passive method.

MCHS with rib-cavity structure is an innovation that can improve the heat transfer performance with less pressure drop in a hybrid MCHS. In 2017, the performance of convergent-divergent channel with ribs and cavities on the sidewall was reported by Srivastava *et al.,* [14] for constant heat flux and Re of 120 – 900. The findings demonstrated that the developed design reduced the overall thermal resistance up to 40% and the temperature of the microchannel bottom surface was relatively uniform. The combined effect of interruption, re-development of the boundary layer and recirculation zone increased the average Nusselt number from 15% to 46% which contributed to the heat transfer augmentation. However, the overall performance of MCHS decreased when the flow rate was increased due to high-pressure drop penalty.

In recent years, the combined effect of cavities and ribs, on the sidewalls and the centre of the straight channel, respectively have gained more attention. Li *et al.,* [15] presented a numerical study to investigate the effects of ribs and cavities on fluid flow and heat transfer characteristics for the Re of 173 to 635. Thermal enhancement factor and entropy generation number augmentation were

used as the performance indicator. The analysis revealed that combined effect of interruption, re-development of the thermal boundary layer, intensified mainstream disturbance, and chaotic mixing between hot and cold water enhanced the heat transfer performance. After a year, Li *et al.,* [16] extended their research using various shapes of ribs and cavities in a straight microchannel and the rib shapes were found to influence thermal and hydraulic performance to a greater extent. Meanwhile, the triangular ribs showed the lowest heat transfer performance compared to other designs although it has the lowest pressure drop penalty due to delayed separation point of the mainstream on the triangular geometry. In contrast, the rectangular rib design has the highest pressure drop penalty among all the designs compared. In the same year, Ghani *et al.,* [17] reported that heat transfer augmentation with a minimal pressure drop in a microchannel with sinusoidal cavities and rectangular ribs can be achieved by geometrical optimisation. The optimum relative cavity amplitude, rib width and rib length found in the study were 0.15, 0.13 and 0.5, respectively. The combination of these optimum parameters resulted in the highest performance factor compared to other designs studied.

In contrast to the aforementioned design configuration, Xia *et al.,* [18, 19] analysed the effects of ribs and cavities at the sidewalls on heat transfer performance using two different methods, namely, Computational Fluid Dynamics (CFD) and CFD with Multi-objective Evolutionary Algorithm (MOEA). In the CFD method, the analysis found that a relative rib height significantly affected entropy generation. Not only that, the combined effect of flow mixing and re-development of the boundary layer in the microchannel increased the heat transfer performance. From the data obtained, Xia *et al.,* [18, 19] established a correlation between Nusselt number and friction factor. Meanwhile, in CFD with MOEA method, the result illustrated that relative rib height increased, thermal resistance and pressure drop penalty decreased and increased, respectively. The relative cavity height and rib height exhibited similar performance trend except for the very deep cavities that could be influenced by the formation of a stagnant zone. Besides, MOEA results indicated a relationship between total thermal resistance and pumping power.

For a better understanding about the effect of geometry configuration or arrangement of ribs and cavities in the straight channel on the thermal performance, Xie *et al.,* [20] developed several designs to analyse the best configuration of rib and cavity combinations. The highest Nusselt number ratio was obtained when using the configuration of ribs on both sidewalls. The Nusselt number ratio decreased according to the following combinations: cavities and ribs on opposite sidewalls > ribs on the sidewall > cavities on the sidewall. For friction factor ratio, ribs on the sidewall and ribs on both sidewalls exhibited the highest values when compared with other configurations.

The most critical issue in the design development of hybrid MCHS is its fabrication process since most of the design of hybrid MCHSs are too complex. Consequently, it is very important to fabricate the proposed hybrid MCHS as there are many limitation during the fabrication process such as the size of cutting tools and micro-machining process. It will determine whether the proposed design can be commercialised and transferred to the mass production in electronic industry or not. Besides that, most of researchers still use straight-channel MCHS for their numerical model validation [16-18, 20, 21] because experimental analyses of the fabricated hybrid MCHS such as regression analysis are very limited in the open literature. Therefore, in this study, hybrid MCHS (TC-RR-SC MCHS) was fabricated and its hydrothermal performance was compared with the simulation result. Regression equations were formulated from the regression analysis, which it can be used as reference for validation purpose in the future study for an innovated MCHS that have similar design with the proposed MCHS.

2. Methodology

There are two essential parts in the present study: the first part describes the numerical approach, and the second part describes the experimental approach for the numerical model validation. According to Figure 1, there are four phases in the research framework: **(1)** Validation of the conventional design of MCHS (CR MCHS) with available data in the previous studies, **(2)** Performing comparative analysis among the enhanced MCHSs, **(3)** Performing PF optimisation and $N_{s,a}$ minimisation through the SC geometries, and **(4)** Validation of numerical model of the proposed MCHS experimentally.
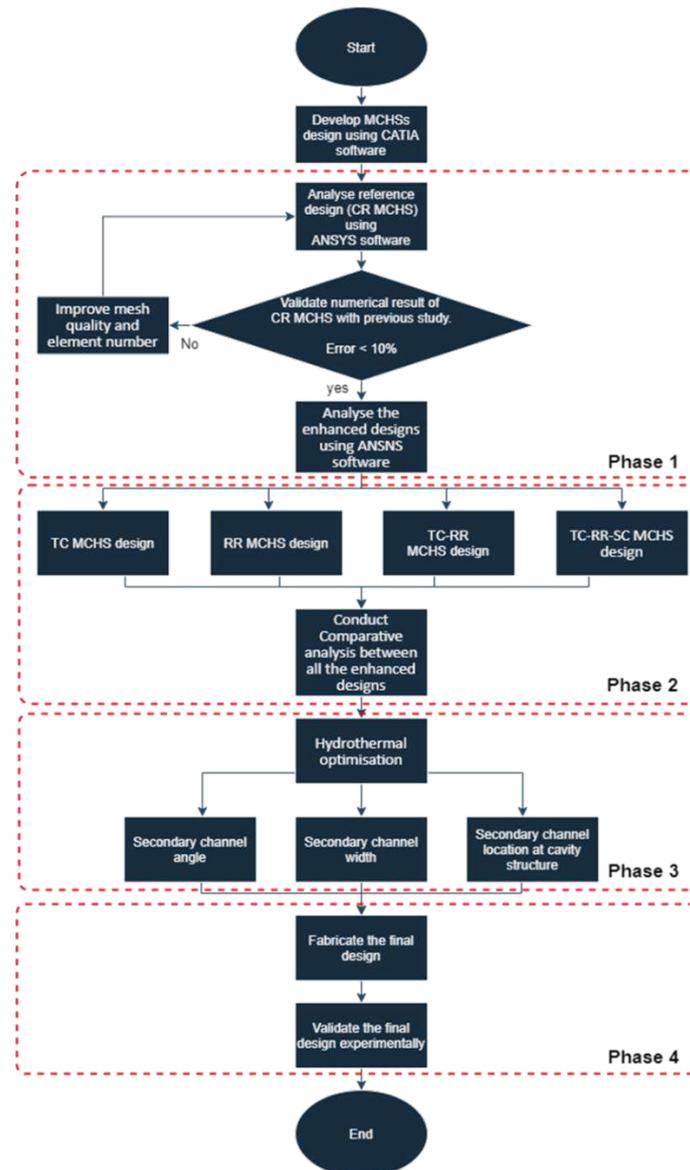

Fig. 1. Flowchart of the research framework

2.1 Numerical Approach
2.1.1 Governing equation

In the present study, the prediction of fluid flow, heat, and mass transfer in all 3D geometry designs were numerically solved by the set of governing mathematical equations, namely, mass,

momentum, and energy conservations, in ANSYS FLUENT 17.0 [22]. The finite volume method was utilised to discretize the governing equation. The SIMPLE algorithm was adopted to accomplish the pressure-velocity coupling. The second-order upwind and second-order central difference schemes were applied for the convective and diffusion terms, respectively. Furthermore, the convergence criteria were set to be less than 10^{-6} for continuity and less than 10^{-9} for energy. The governing equations were solved according to the following assumptions:

I.   Fluid is incompressible and Newtonian.
II.   Knudsen number (Kn) of water in microfluidic channels is less than 10^{-3}. Therefore, fluid flow is assumed as a continuum. At this condition, the non-slip boundary condition and the Navier-stokes equation are applicable [15].
III. The flow region is laminar.
IV.   Both fluid flow and heat transfer processes are in a steady-state condition.
V.   Gravitational force, viscous dissipation and radiation heat transfer are neglected.
VI.   Thermophysical properties of the fluid are constant.

By applying the assumptions in the governing equations, the conservation of mass, momentum and energy can be rewritten as Eq. (1), Eqs. (2) to (4), and Eqs. (5) to (6), respectively:

Continuity equation:

$$\frac{\partial u}{\partial x} + \frac{\partial v}{\partial y} + \frac{\partial w}{\partial z} = 0 \tag{1}$$

Where u, v and w are the velocity components in x, y and z-directions respectively.

Momentum equations:

$$u\frac{\partial u}{\partial x} + v\frac{\partial u}{\partial y} + w\frac{\partial u}{\partial z} = -\frac{1}{\rho_f}\frac{\partial P}{\partial x} + \frac{\mu_f}{\rho_f}\left(\frac{\partial^2 u}{\partial x^2} + \frac{\partial^2 u}{\partial y^2} + \frac{\partial^2 u}{\partial z^2}\right) \tag{2}$$

$$u\frac{\partial v}{\partial x} + v\frac{\partial v}{\partial y} + w\frac{\partial v}{\partial z} = -\frac{1}{\rho_f}\frac{\partial P}{\partial y} + \frac{\mu_f}{\rho_f}\left(\frac{\partial^2 v}{\partial x^2} + \frac{\partial^2 v}{\partial y^2} + \frac{\partial^2 v}{\partial z^2}\right) \tag{3}$$

$$u\frac{\partial w}{\partial x} + v\frac{\partial w}{\partial y} + w\frac{\partial w}{\partial z} = -\frac{1}{\rho_f}\frac{\partial P}{\partial z} + \frac{\mu_f}{\rho_f}\left(\frac{\partial^2 w}{\partial x^2} + \frac{\partial^2 w}{\partial y^2} + \frac{\partial^2 w}{\partial z^2}\right) \tag{4}$$

Where ρ_f and μ_f are the density and dynamic viscosity of the working fluid, respectively, and P is the pressure of the fluid.

Energy equation for the fluid:

$$u\frac{\partial T_f}{\partial x} + v\frac{\partial T_f}{\partial y} + w\frac{\partial T_f}{\partial z} = \frac{k_f}{\rho_f c_{pf}}\left(\frac{\partial^2 T_f}{\partial x^2} + \frac{\partial^2 T_f}{\partial y^2} + \frac{\partial^2 T_f}{\partial z^2}\right) \tag{5}$$

Where T_f is the fluid temperature, c_{pf} is fluid specific heat and k_f is fluid thermal conductivity.

Energy equation for the solid region:

$$\frac{\partial^2 T_s}{\partial x^2} + \frac{\partial^2 T_s}{\partial y^2} + \frac{\partial^2 T_s}{\partial z^2} = 0 \qquad (6)$$

where T_s is solid temperature.

2.1.2 Data acquisition

The relevant expressions used in the present study to investigate the fluid flow and heat transfer characteristics as follows:

$$\text{Re} = \frac{\rho_f u_m D_h}{\mu_f} \qquad (7)$$

Where u_m and D_h are mean velocity and hydraulic diameter, respectively. The D_h was calculated by Eq. (8) [23].

$$D_h = \frac{2HcWc}{Hc + Wc} \qquad (8)$$

The following equation calculated the average apparent friction factor [24].

$$f_{app,ave} = \frac{2D_h \Delta P}{Lt \rho_f u_m^2} \qquad (9)$$

The average convective heat transfer coefficient and Nusselt number were calculated by the Eq. (10) [23] and Eq. (11) [25], respectively.

$$h_{ave} = \frac{q_w A_{film}}{A_{conv.}(T_{w,ave} - T_{f,ave})} \qquad (10)$$

$$Nu_{ave} = \frac{h_{ave} D_h}{k_f} \qquad (11)$$

Where A_{film} and $A_{conv.}$ are the heated and convective heat transfer areas, respectively. The q_w is the applied heat flux at the bottom surface of the MCHS. The $T_{w,ave}$ and $T_{f,ave}$ are the average temperature of microchannel wall and fluid, respectively.

2.2 Experimental Approach

The experimental study was conducted in order to measure the average Nusselt number, Nu_{ave}, and friction factor, f_{app}, in the fabricated TC-RR-SC MCHS for the validation purpose. In the present study, distilled water was used as a coolant in the fabricated TC-RR-SC MCHS. The details of the test

rig, experimental setup, and apparatus specification that were used in the present study are discussed in the next sections.

2.2.1 Test rig

There are five main parts in the test rig device, namely, manifold, aluminium block, top cover, base, and cartridge heater holder, as shown in Figure 2(b). The top cover was used as insulator to prevent heat dissipates from the top surface of the fabricated MCHS to outside of the test rig. The top cover is made of transparent polycarbonate (Lexan), which has low thermal conductivity (0.2 W/m-K). The design and material selection of manifold is very crucial as it affects the flow distribution and characteristics in microchannels. In the present study, the manifold is made of acetal (Polyoxymethylene, POM). The material is highly recommended in the fabrication of high precision part due to having a high stiffness, low friction and dimensional stability. Two T-type pipe connectors were connected to the inlet and outlet ports of the manifold in order to guide coolant to enter and leave manifold continuously, as shown in Figure 3(b). Besides that, five thermocouple holders were connected to the manifold. Two thermocouples were used to measure the inlet and outlet temperatures. The other three thermocouples were used to measure the aluminium block temperature.

Besides the manifold, the cartridge heater holder and base are also made of acetal in order to prevent heat generated by heaters dissipate to outside of the test rig. The aluminium block can be divided into three parts, namely, upper, middle, and lower bodies, as illustrated in Figure 4(a). The optimised TC-RR-SC MCHS was machined on the top surface of the upper body by a micro-milling machine. The middle body was used as a holder between the aluminium block and manifold. Four holes with a height of 39 mm were drilled across the lower body, as shown in Figure 4(b). Those holes were inserted with four cartridge heaters (OMEGA-HDC00024-250W-240V) in order to supply heat to the aluminium block.
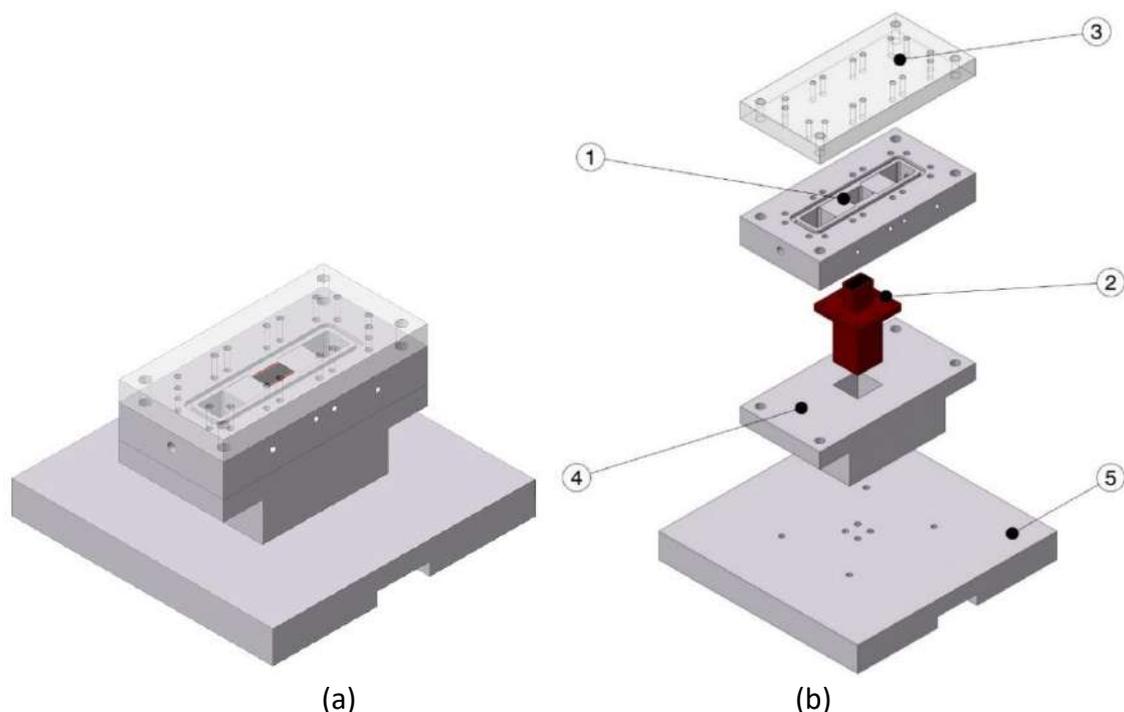

(a)	(b)

Fig. 2. The test rig of the optimised TC-RR-SC MCHS (a) Test rig design (b) Exploded view of test rig
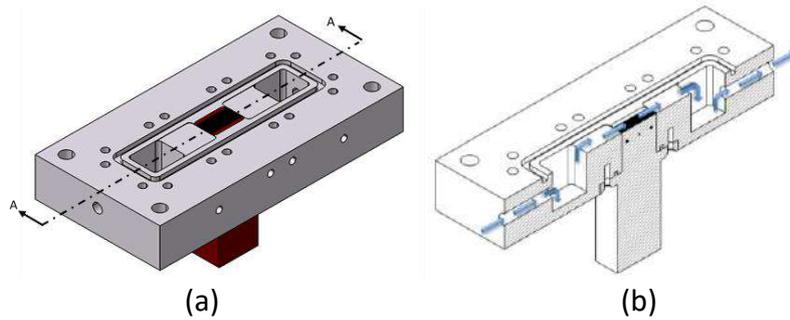
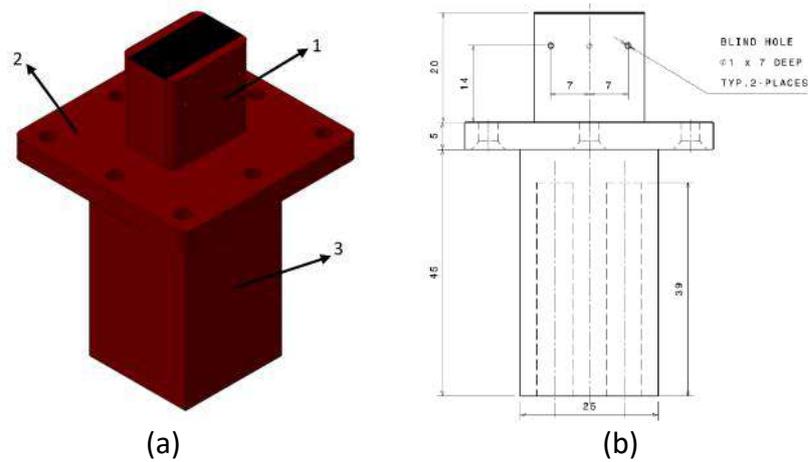**Fig. 3.** Manifold with aluminium block (a) Isometric view (b) A-A cross-section

Fig. 4. Aluminium block (a) Isometric view (b) Dimensional drawing

2.2 Apparatus Specification

Table 1 shows the list of apparatus that were used in the experimental setup, as illustrated in Figure 5. There are three main components in this experimental setup: **(1)** Thermocouple for the MCHS temperature measurement; **(2)** Pressure transducer for the pressure drop, ΔP, measurement in microchannels; and **(3)** Flow meter for the flow rate measurement. These three components had been calibrated first before they were used in the present experiment.
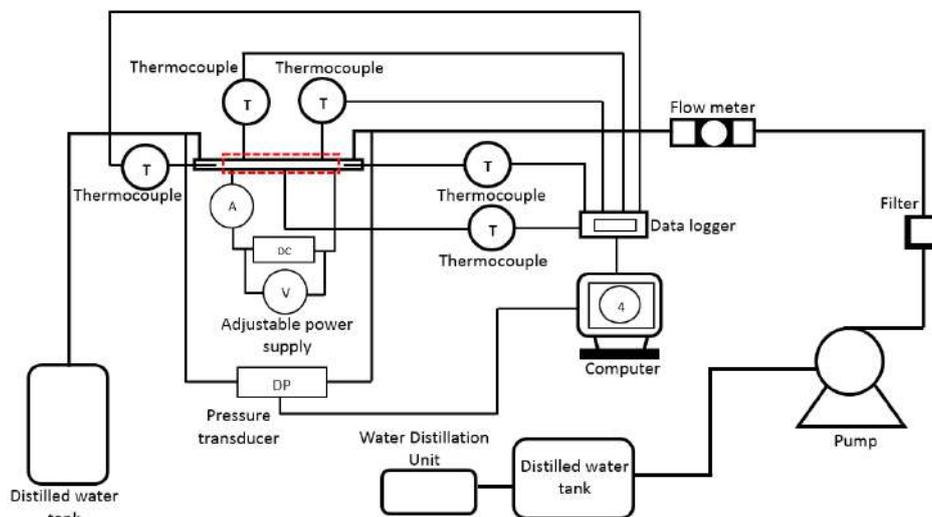

Fig. 5. Schematic diagram of the experimental setup

Table 1

Apparatus specification

Apparatus	Model and Specification
Water Distillation unit	**Favorit W4L** • Power supply: 220-240 V; 50/60 Hz; Single phase • Water Supply Requirement: 1 litre/min • Distillate output: 4 litres per hour, single distilled
Adjustable Pump	**Peristaltic Pump: FPU500** Flow Rate: 0.5~2280 ml/min **Pump Motor: FPU5-MT-220** • Maximum Back Pressure: 137.9 kPa • Pumpsil Tubing Wall: 1.5 mm (1/16") • Fluid Temperature Range: -46~ 149 °C
Pressure transducer	**OMEGA-MMDWU030-USBHK3ME0T8A6CE** • Range: 200 kPa • Accuracy: +/-0.08%
Flow meter	**FLR1009-D** • Flow Range: 10 to 500 ml/min • Max Pressure Drop: 68.9 kPa
Thermocouple	**TJ40-CPSS-040G** • Type: T • Sheath diameter: 1 mm • Upper temperature: 260 °C
Data logger	**LR8431-20** Power Sources: 100 to 240 V AC; 50/60 Hz using AC Adapter Z1005
Regulated DC power supply	**APS3005DM** Input: 220 V±10% 50Hz Output: 0~30 V regulable; 0~5 A regulable
Cartridge heaters	**OMEGA-HDC00024W-240V** Sheath Length: 38.1 mm Power: 250 watts Voltage: 240 V
Filter	**Swagelok-SS-4TF-LE** Pore size: 15 micron

2.3 Experimental Procedures

Figure 6 shows the actual experimental setup in this study. These experiments consist of three main processes such as distilled water preparation, heating process and fluid flow process. In the preparation of distilled water, a water distillation unit was used to prepare 25 Liters distilled water. The heating process is a process to apply heat flux on the aluminium block body. Four cartridge heaters generated the heat flux of 58804.41 W/m^2 to the upper body of aluminium block. The temperature changes of fluid and microchannel walls were measured by five thermocouples Type-T connected to the manifold. Two thermocouples (T_1 and T_4) were used to measure the fluid temperature at inlet and outlet of MCHS (In the deep plenum), while other three thermocouples (T_2, T_3 and T_5) were used to measure the wall temperature of MCHS at the three different locations, as shown in Figure 7.

In the fluid flow process, peristaltic pump and flow meter were used to control the volume flow rate in the fabricated MCHS. In contrast, a filter with the pore size of 15 microns was used to filter any particle that may clog the fluid flows in the fabricated MCHS. Pressure drop in the fabricated MCHS was not measured directly at the inlet and outlet of the MCHS, since the pressure transducer

was connected to both T-type pipes, as shown in Figure 7. The actual pressure drop in the fabricated MCHS was measured by considering the pressure loss due to contraction and expansion effects in the manifold structure. The details of the pressure drop measurements are discussed in the next section.
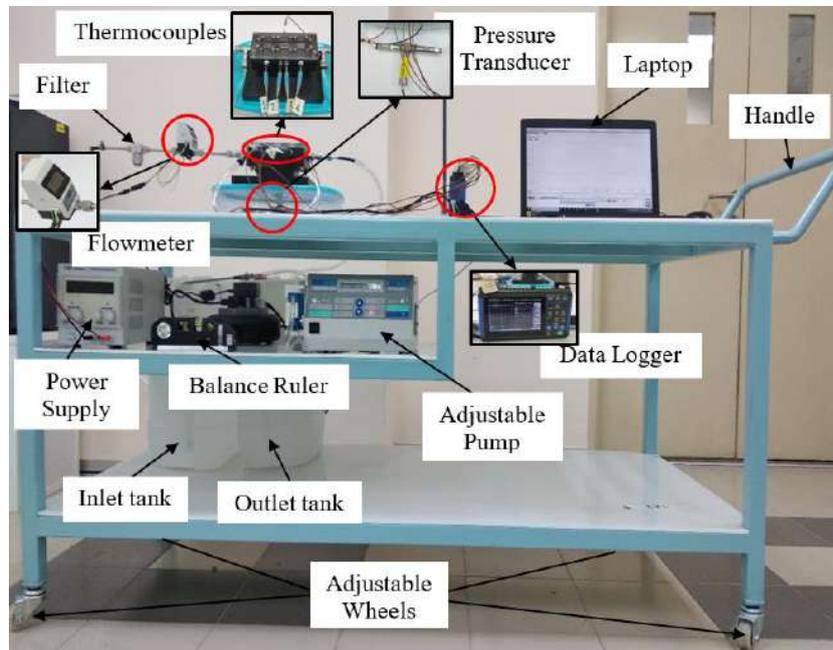

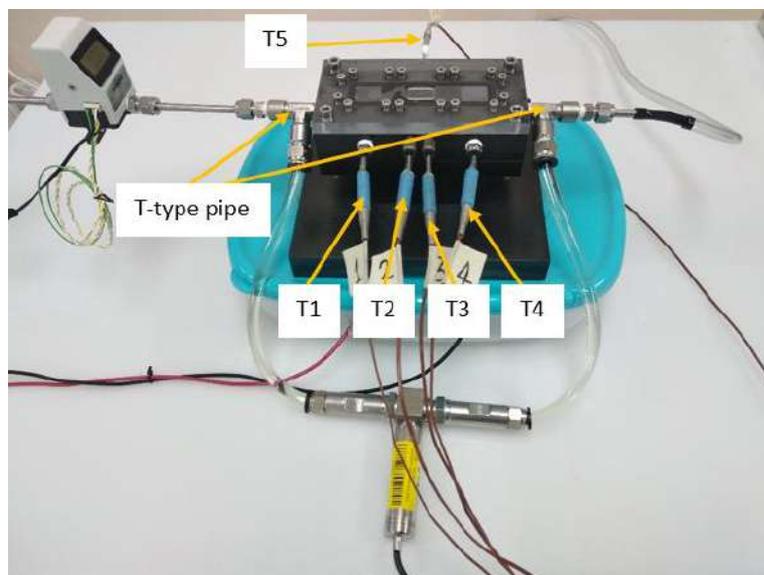**Fig. 6.** Experiment apparatus with adjustable table

Fig. 7. Front view of TC-RR-SC MCHS device

Before the experiment started, the tube size and volume flow rate had been adjusted in the adjustable pump system according to the diameter of pumpsil tube. Next, the distilled water had been primed by the adjustable pump to flow through the peristaltic pump, filter and flow meter in the series arrangement before it entered to the manifold inlet (as shown in Figure 8). After that, the distilled water had been being collected by the outlet tank until the experiment was completed. After all the channels had been filled with the distilled water without any bubble issues, the experiment was started.
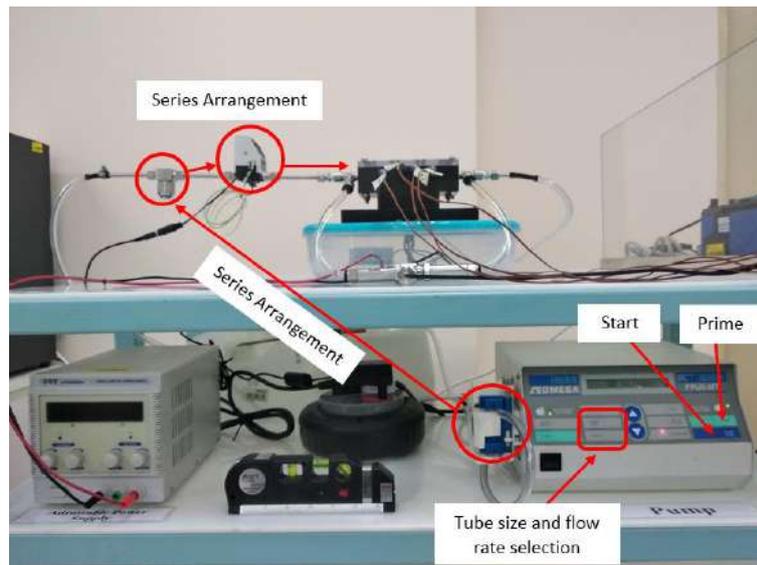
Fig. 8. Fluid flow process setup

The volume flow rate was set to the desired value. Next, the power supply of the cartridge heaters was switched on, after the flow rate had reached its stable conditions (as shown in Figure 9). The measurement of temperature changes and pressure drop had been being recorded until the temperature reading reached the steady-state condition, as illustrated in Figure 10. Usually, the steady-state condition is achieved in 35–60 minutes. The steady-state value of each thermocouple and pressure transducer readings were calculated based on the average of 1000 readings sampled at 1000 seconds.
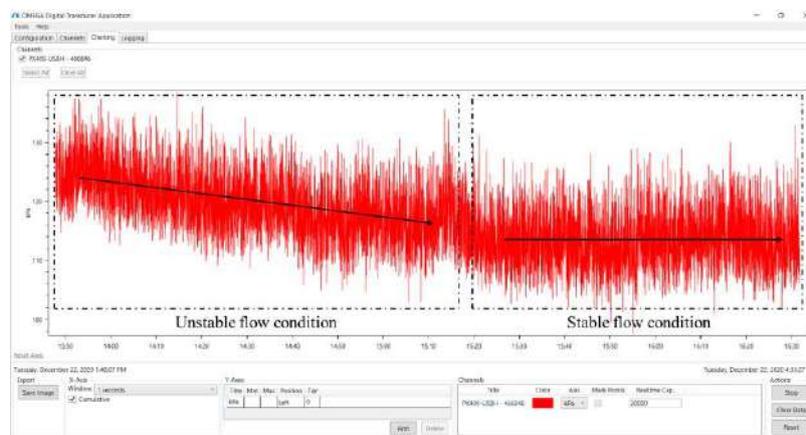

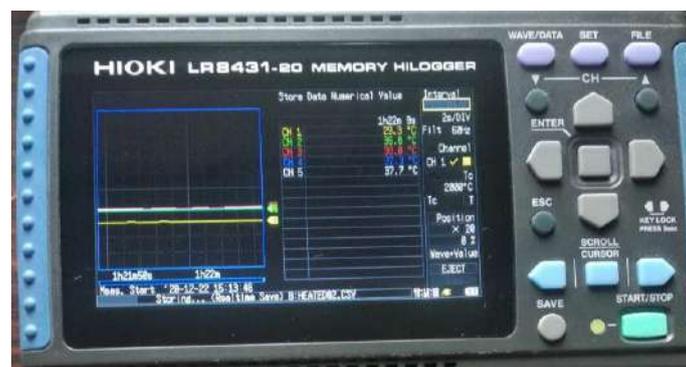**Fig. 9.** Pressure transducer reading for the stable flow rate condition

Fig. 10. Temperature reading for the steady-state condition

2.4 Data Reduction

There are two main parameters in the experimental analysis, such as the average Nusselt number, Nu_{ave}, and friction factor, f_{app}. In this section, the relevant expressions related to those parameter measurements are discussed in detail. Figure 11 shows the flow chart of the average Nusselt number calculation.
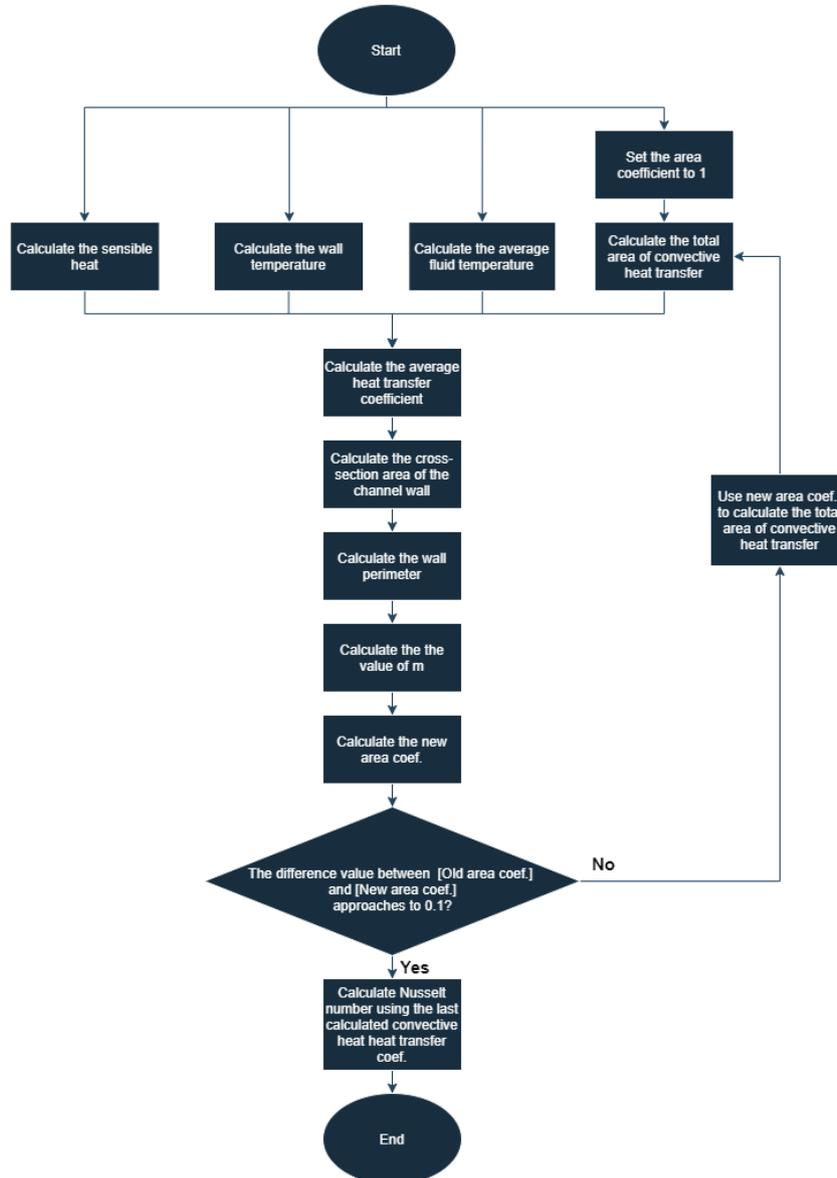

Fig. 11. Flow chart of the average Nusselt number calculation

Before the Nu_{ave} was calculated, the average convective heat transfer coefficient, h_{ave}, had been determined first based on the sensible heat, the average wall and fluid temperatures, and the total area of convective heat transfer. The Nu_{ave} and h_{ave} equations are shown in Eq. (12) and Eq. (13), respectively.

$$Nu_{ave} = \frac{h_{ave}D_h}{k_f}$$

(12)

$$h_{ave} = \frac{Q_{sen}}{A_t \left(T_w - T_{f,ave} \right)} \tag{13}$$

Where Q_{sen} is sensible heat gained by the distilled water from the fabricated MCHS. The Q_{sen} value was calculated by the energy balance, as shown in Eq. (14).

$$Q_{sen} = \rho_f c_{pf} \dot{V} \left(T_4 - T_1 \right) \tag{14}$$

The volume flow rate, $\dot{V}$, of the distilled water was measured experimentally via a flow meter. The inlet and outlet temperatures of the distilled water in the fabricated MCHS were measured by the T_1 and T_4 thermocouples, respectively, as illustrated in Figure 7. The total area of convective heat transfer, A_t, was calculated by the following equation:

$$A_t = A_{bc} + \eta A_{fin} \tag{15}$$

Where A_{bc} is the unfinned area at the bottom surface of microchannels, while A_{fin} is the fin area. Both parameters were measured directly from the geometry design of the optimised TC-RR-SC MCHS in the CATIA software. The tip of the sidewalls and rib geometries were assumed in an adiabatic tip condition as the top cover of the TC-RR-SC MCHS device is made of a low-conductivity material (0.2 W/m-K). Thus, the coefficient of area, η, can be written as [26]:

$$\eta = \frac{\tanh\left(mHc\right)}{mHc} \tag{16}$$

$$m = \sqrt{\frac{h_{ave} P_w}{k_{al} A_c}} \tag{17}$$

Where P_w, k_{al}, and A_c are the wall perimeter, the thermal conductivity of Aluminium 6061 T6 (167 W/m-k), and the cross-section area of the channel wall, respectively. The P_w and A_c values were calculated by Eq. (18) and Eq. (19), respectively.

$$P_w = 2Hc + W_w \tag{18}$$

$$A_c = Hc W_w \tag{19}$$

The W_w represents the thickness of the channel wall. The final value of the convective heat transfer coefficient was determined after the total area of convective heat transfer had been being calculated by the iterative approach. Firstly, the initial value of η_{old} was set to 1 in order to compute the h_{ave} value in Eq. (13). Secondly, the calculated h_{ave} value was substituted in Eq. (17) to calculate the value of m. Finally, the m value was substituted in Eq. (16) to calculate the new coefficient of area, η_{new}. This process had been being repeated until the difference between η_{old} and η_{new} approached to 0.1.

The average fluid temperature, $T_{f,ave}$, and wall temperature, T_w in Eq. (13) were calculated by the Eq. (20) and Eq. (21), respectively. As illustrated in Figure 12, the direct measurement of T_w is not available. Thus, extrapolation of the measured temperatures (T_2, T_3 and T_5) were performed by assuming 1D heat conduction [27]. This assumption is valid for a material with high thermal conductivity and insulated walls of MCHS.

$$T_{f,ave} = \frac{T_1 + T_4}{2} \tag{20}$$

$$T_w = T_{al} - \frac{Sq_{w,s}}{k_{al}} \tag{21}$$

Where T_{al} is the average temperature (T_2, T_3 and T_5) of aluminium block. The vertical distance between those thermocouples and the bottom surface of the microchannel, S, is 5.8 mm. The supplied heat flux in the aluminium block was calculated as the sensible heat, Q_{sen}, gained by the distilled water over the base area of the aluminium block upper body, A_{ubb}, as shown in Eq. (22).

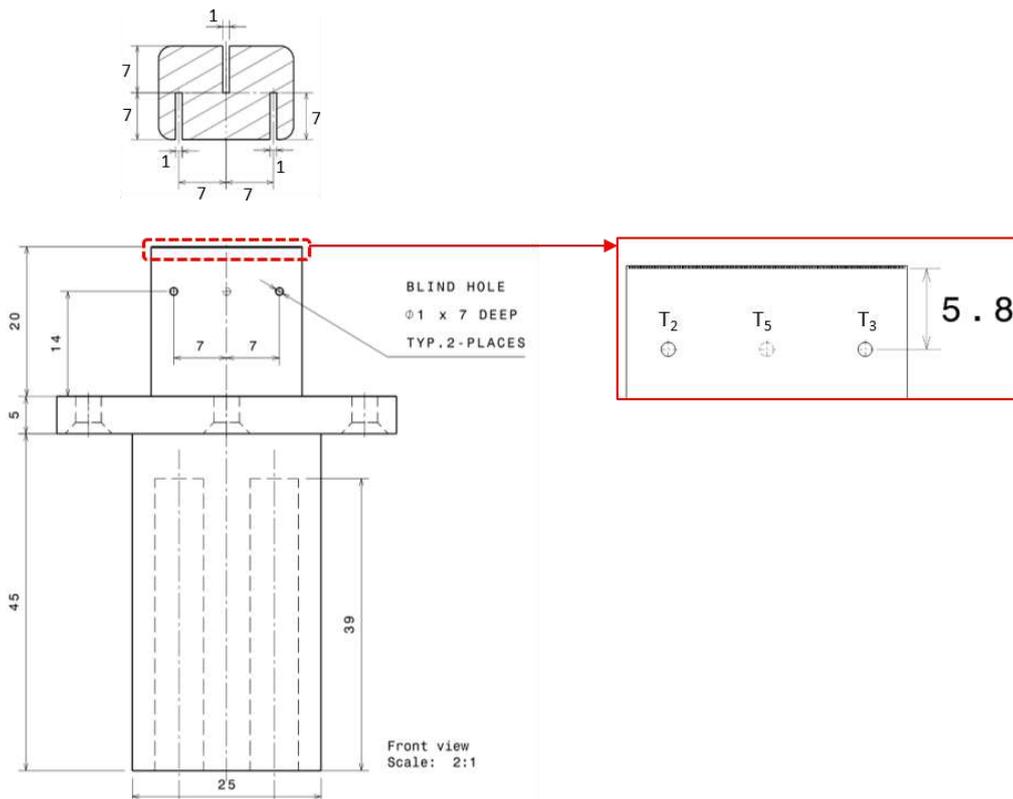$$q_{w,s} = \frac{Q_{sen}}{A_{ubb}} \tag{22}$$

Fig. 12. The locations of three thermocouples in the upper body of the aluminium block (All dimensions in mm)

The velocity of the distilled water, U, in the TC-RR-SC MCHS device was calculated by the following equation:

$$\text{Re} = \frac{\rho_f U D_h}{\mu_f} \tag{23}$$

All the distilled water properties (ρ_f, μ_f, c_{pf} and k_f) were determined by the average fluid temperature, $T_{f,ave}$, in the following formulas [26]:

Density:

$$\rho_f = \frac{a_0 + a_1(T_{f,ave}) + a_2(T_{f,ave})^2 + a_3(T_{f,ave})^3 + a_4(T_{f,ave})^4 + a_5(T_{f,ave})^5}{1 + b(T_{f,ave})} \tag{24}$$

Where;

$a_0 = 999.8396$
$a_1 = 18.22494$
$a_2 = -7.92221 \times 10^{-3}$
$a_3 = -5.54485 \times 10^{-5}$
$a_4 = 1.49756 \times 10^{-7}$
$a_5 = -3.93295 \times 10^{-10}$
$b = 1.81597 \times 10^{-2}$

In the density calculation, the $T_{f,ave}$ value is in degree Celsius (°C).

Thermal conductivity:

$$k_f = -0.58166 + 6.3555 \times 10^{-3}(T_{f.ave}) - 7.9643 \times 10^{-6}(T_{f.ave})^2 \tag{25}$$

Specific heat capacity:

$$c_{pf} = 8958.9 - 40.535(T_{f,ave}) + 0.11243(T_{f,ave})^2 - 1.0138 \times 10^{-4}(T_{f,ave})^3 \tag{26}$$

Dynamic viscosity:

$$\mu_f = 2.414 \times 10^{-5} \times 10^{\left(\frac{247.8}{T_{f,ave}-140}\right)} \tag{27}$$

The unit of $T_{f,ave}$ should be in Kelvin (K) for the thermal conductivity, specific heat capacity and dynamic viscosity calculations.

In the present experimental setup, the pressure transducer was not directly connected to the inlet and outlet of the microchannels, as shown in Figure 7. Thus, the pressure transducer measured the total pressure loss, ΔP_{tot}, in both manifold and fabricated MCHS, as shown in Eq. (28):

$$\Delta P_{tot} = \Delta P_{mchs} + \Delta P_{se} + \Delta P_{sc} \tag{28}$$

Where ΔP_{mchs} is the actual pressure drop in the fabricated MCHS. Pressure loss due to sudden expansion and contraction is denoted by ΔP_{se}, and ΔP_{sc}, respectively. There are three equations for each ΔP_{se} and ΔP_{sc} according to Figure 13. The equations can be written as follows:

Pressure loss due to sudden expansion, ΔP_{se}:

$$\Delta P_{1-2} = \frac{1}{2} \rho_f \left(u_2{}^2 - u_1{}^2 \right) + \frac{K_{e1}}{2} \rho_f u_1{}^2 \tag{29}$$

$$\Delta P_{4-5} = \frac{1}{2} \rho_f \left(u_5{}^2 - u_4{}^2 \right) + \frac{K_{e2}}{2} \rho_f u_4{}^2 \tag{30}$$

$$\Delta P_{5-6} = \frac{1}{2} \rho_f \left(u_6{}^2 - u_5{}^2 \right) + \frac{K_{e3}}{2} \rho_f u_5{}^2 \tag{31}$$

Velocity in the cross-section of 1, 2, 4, 5 and 6 areas are denoted by u_1, u_2, u_4, u_5, and u_6, respectively. The loss coefficient of the sudden expansion values (K_{e1}, K_{e2}, and K_{e3}) were determined from the Handbook of Heat Transfer [28].

Pressure loss due to sudden contraction, ΔP_{sc}:

$$\Delta P_{2-3} = \frac{1}{2} \rho_f \left(u_3{}^2 - u_2{}^2 \right) + \frac{K_{c1}}{2} \rho_f u_3{}^2 \tag{32}$$

$$\Delta P_{3-4} = \frac{1}{2} \rho_f \left(u_4{}^2 - u_3{}^2 \right) + \frac{K_{c2}}{2} \rho_f u_4{}^2 \tag{33}$$

$$\Delta P_{6-7} = \frac{1}{2} \rho_f \left(u_7{}^2 - u_6{}^2 \right) + \frac{K_{c3}}{2} \rho_f u_7{}^2 \tag{34}$$

Where u_3 and u_7 are velocity values in the cross-section of 3 and 7. The loss coefficient of sudden contraction values (K_{c1}, K_{c2}, and K_{c3}) were also could be found in the Handbook of Heat Transfer [28].
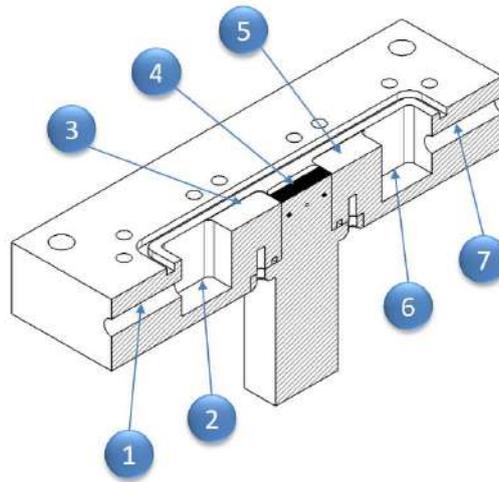
Fig. 13. Flow trajectory through different regions
of the manifold and the MCHS

The friction factor, f_{app}, in the fabricated MCHS was measured by substituting the calculated ΔP_{mchs} in the Eq. (35).

$$f_{app} = \frac{2\Delta P_{mchs}D_h}{\rho LtU^2} \tag{35}$$

2.5 Preliminary Study

The preliminary study was conducted to determine the point where the variables are within the acceptable range based on the device specifications and the tube materials used in the present experiments. Besides that, this preliminary study was conducted to ensure the whole experiments were performed in the control environment. The tube selection is very important for the fluid transportation since it affects the fluid flow characteristics. As seen in Figure 14, when the silicon tube was used as a fluid transportation, the flow of the distilled water decreased over time as illustrated by the pressure transducer reading in Figure 14(a). As consequence, it affected the MCHS temperature as less coolant flows in its channels. In order to control the accuracy of the experimental result, a pumpsil tube (6.4 mm bore × 1.6 mm thickness) was used as a new fluid transportation (see Figure 14(b)). By using this pumpsil tube, the experiments were able to run up to 3 hours before the peristaltic pump loss its power due to the extra of 0.1 mm wall thickness of the used pumpsil tube. According to a manual provided by the peristaltic pump manufacturer (OMEGA Engineering), a pumpsil tube of 1.5 wall thickness should be installed in the peristaltic pump. However, the manufacturer does not supply the pumpsil tube anymore since the FPU500 peristaltic pump has been discontinued from its production.

When the peristaltic pump loss its power, the rotation of roller shaft (see Figure 15) became inconsistent and, consequently, produced unstable flow of distilled water to the TC-RR-SC MCHS device.

Table 2 shows the summary of the limit test conditions for equipment used in the present study. According to the flow meter specification, this test was started with 44 ml/min flow rate. The tests showed that all the equipment was in a good condition except for the pressure transducer, peristaltic pump, and pumpsil tube at the flow rate of 250 ml/min. At this flow rate, the pressure transducer did not measure the pressure difference in the TC-RR-SC MCHS device correctly as shown in Figure

16(a). Besides that, the fuse of the peristaltic pump was blown, and the pumpsil tube was burst due to the excessive pressure generated by this flow rate (see Figure 16(b) and Figure 16(c)).
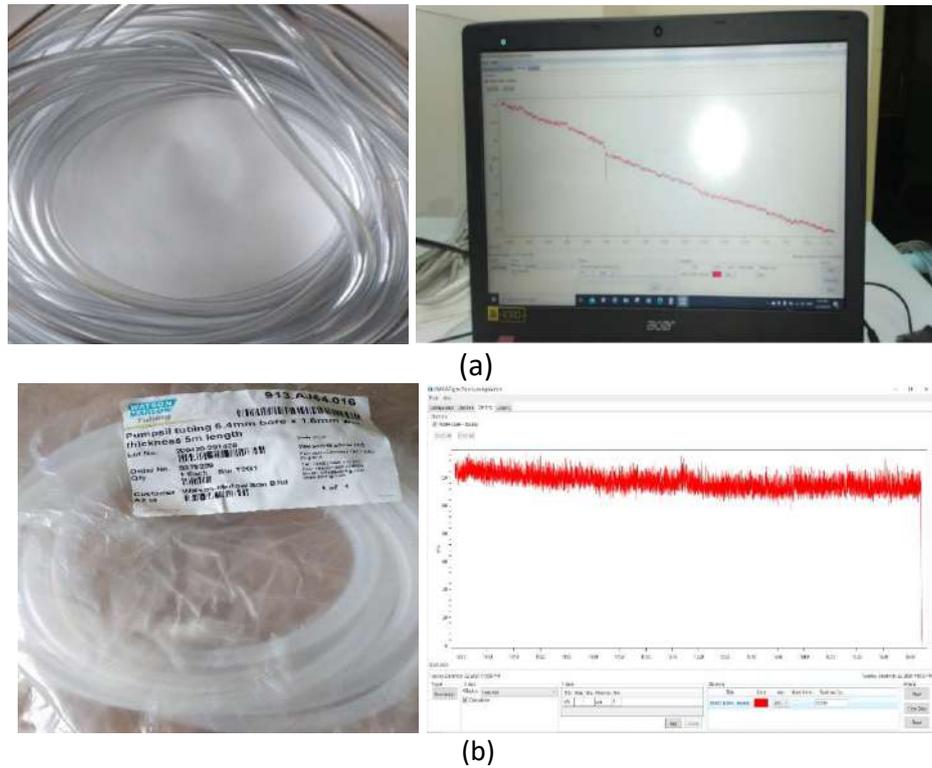

(a)

(b)

Fig. 14. Tube selection for the fluid transportation: (a) Silicon tube, and (b) Pumpsil tube
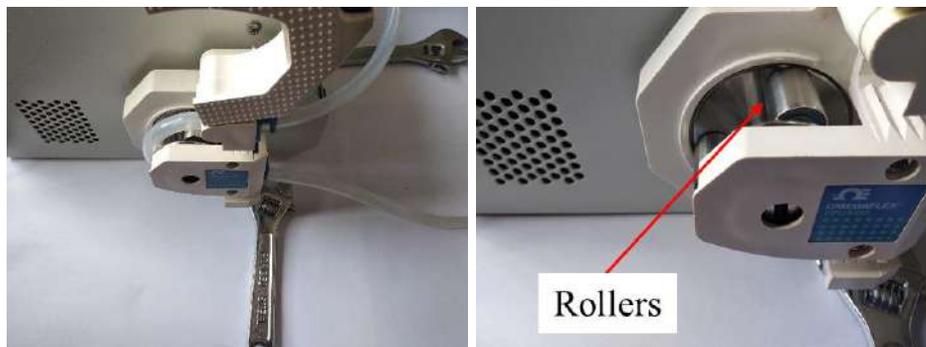

Fig. 15. Peristaltic pump (a) with pumpsil tube, (b) without pumpsil tube

Table 2
Equipment limit test conditions

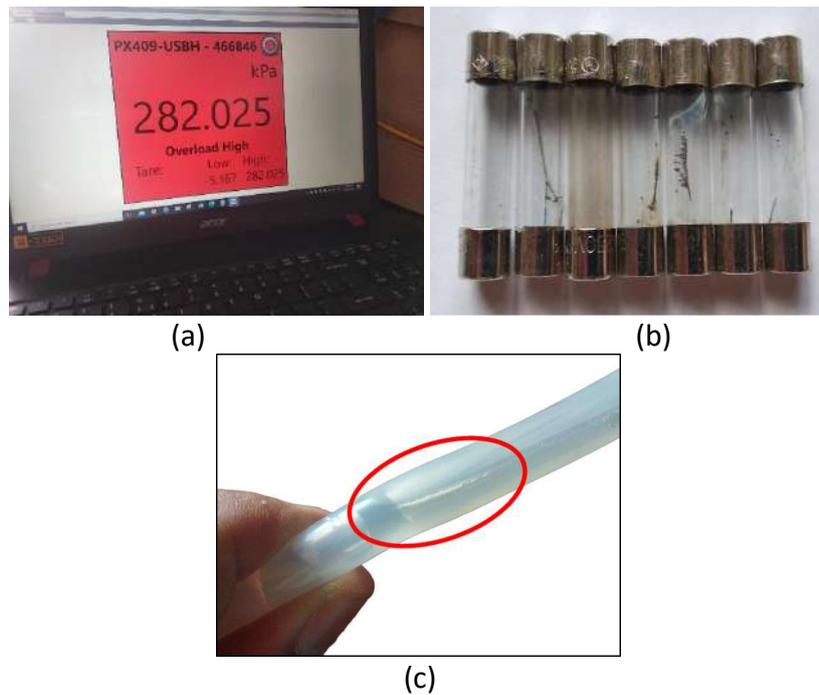| Equipment	Flow Rate (ml/min)					
	44	88	130	170	230	250
Thermocouples	Good	Good	Good	Good	Good	Good
Pressure transducer	Good	Good	Good	Good	Good	Overload (<200 kPa)
Flow meter	Good	Good	Good	Good	Good	Good
Peristaltic pump	Good	Good	Good	Good	Good	Fuse blown out
Pumpsil tube	Good	Good	Good	Good	Good	burst out

Fig. 16. Effect of high volume flow rate (<50 ml/min): (a) Overload reading on pressure transducer, (b) Blown pump fuse, (c) Burst pumpsil tube

After considering all the factors involved in this preliminary study, the range of flow rate of 44 ml/min – 230 ml/min (100≤Re≤500) was set to all experiment runs in order to prevent or minimise the failure of equipment used. Besides that, each experiment run was conducted up to 3 hours only before the next experiment run. This duration was considered acceptable for ensuring the experiments can produce consistent, reproducible, and reliable results.

3. Results and Discussion

Experimental analysis was conducted in order to validate the numerical model of TC-RR-SC MCHS experimentally. This validation was conducted in order to measure the deviation of result between the simulation and experimental involved in this study. Hence, this analysis can be used as a reference for future study in the comparison of hybrid MCHS performance. Besides that, this experimental set up can be used for the other designs as the block of the TC-RR-SC MCHS can be slotted out and replaced with the other block of MCHS. The fabricated TC-RR-SC MCHS is made of aluminium 6061 T6. There are two parameters in the validation process, namely, Nu_{ave} and f_{app}. Before the experiment had been started, the uncertainties analysis was conducted first in order to ensure the measured values within which the true value of the measurement lies. It is discussed further in the next sub-section.

3.1 Uncertainties Analysis

Uncertainty analysis was conducted in order to calculate the range of possible values within which the true value of the measurement lies. There are two main errors that contributed to the uncertainty of measurement in the present experiment: (1) Random or precision errors, and (2) Systematic or bias errors.

According to Coleman *et al.,* [29], the main factor that contributes to the random errors are unsteady influences. This unsteady influences cause the scattered data in measurements and they only can be revealed by repeating a measurement over an appropriate time interval. Therefore, the random errors can be analysed statistically. However, the systematic errors cannot be analysed statistically as the errors of inaccuracies are reproducible consistently in the same direction. As a result, the errors are difficult to be detected. External sources such as the imperfection of instruments and environmental errors become the major factors that contribute to the systematic errors. This systematic error can be minimised by calibration against a standard system in order to develop a correction of correlation.

In the present experiment, both random (precision, *Pr*) and systematic (bias, *Br*) errors were measured in order to calculate the overall uncertainties of a parameter, r. The overall uncertainties of U_r can be calculated by the following equations.

$$U_r = \sqrt{P_r^2 + B_r^2} \tag{36}$$

The uncertainties of a parameter, r with the measured variable of X can be written as follows:

$$Pr = r\left(X_1, X_2, X_3, ..., X_j\right) \tag{37}$$

$$Br = r\left(X_1, X_2, X_3, ..., X_j\right) \tag{38}$$

The random error propagation and the bias uncertainty of r were calculated by Eq. (39) and Eq. (40), respectively.

$$P_r^2 = \left(\frac{\partial r}{\partial X_1}\right)^2 P_{X_1}^2 + \left(\frac{\partial r}{\partial X_2}\right)^2 P_{X_2}^2 + ... + \left(\frac{\partial r}{\partial X_j}\right)^2 P_{X_j}^2 \tag{39}$$

$$B_r^2 = \left(\frac{\partial r}{\partial X_1}\right)^2 B_{X_1}^2 + \left(\frac{\partial r}{\partial X_2}\right)^2 B_{X_2}^2 + ... + \left(\frac{\partial r}{\partial X_j}\right)^2 B_{X_j}^2 \tag{40}$$

Table 3 presents the uncertainties of the measurable parameters in the experiment.

Table 3
The Uncertainties of the measurable parameters in experiment

Parameter	Uncertainty
Heat flux	3.6%
Thermal energy	2.7%
Hydraulic diameter	4.5%
Flow rate	0.9%
Power supply	0.8%
Pressure transducer	0.5%

3.2 Formulation of the Regression Equations of Hydrothermal Performance

There are two important parameters in the evaluation of hydrothermal performance: (1) Nusselt number, Nu_{ave}, and (2) Friction factor, f_{app}. Figure 17 shows the experimental result of Nu_{ave} for the Re of 100 to 500. Based on the correlation analysis, the correlation coefficient, r for the experimental result of Nu_{ave} was 0.98. It indicated that there was a significant positive relationship between Re and Nu_{ave} ($r(7)=.98$, $p<.05$).

Besides that, regression analysis was also conducted in order to formulate regression equations. This equation can be used by other researchers for validation purpose for those who study a similar design as TC-RR-SC MCHS. The analysis showed that the R² value for this analysis was 0.9514. It demonstrated that 95% of the variability in Nu_{ave} was explained by the variability in Re. Eq. (41) is the regression equation of the Nu_{ave}.

$$Nu_{ave} = 0.042 \, (\text{Re}) + 6.0191 \tag{41}$$
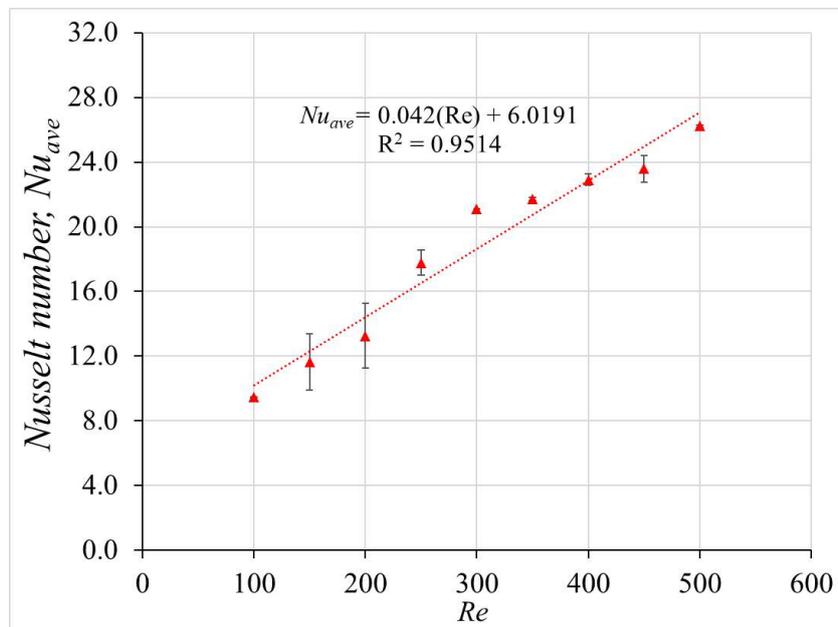

Fig. 17. Experimental result of the Nusselt number, Nu_{ave} of the optimised TC-RR-SC MCHS

Similar to the experimental result of the Nu_{ave}, f_{app} also showed a significant negative relationship to the Re (see Figure 18). The correlation coefficient of the experimental result of friction factor, f_{app} was -0.95 ($r(7)=-.95$, $p<.05$). The regression analysis also demonstrated that 90% of the variability in f_{app} was explained by the variability in Re (R² = 0.9037). Eq. (42) is the regression equation of the friction factor, f_{app} that formulated in this analysis.

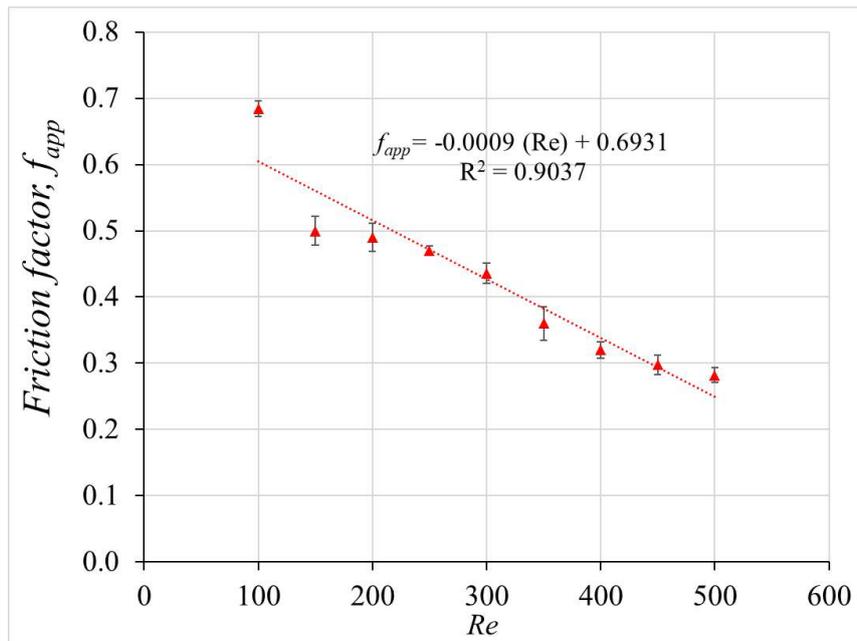$$f_{app} = -0.0009 \, (\text{Re}) + 0.6931 \tag{42}$$

Fig. 18. Experimental result of the friction factor, f_{app} of the optimised TC-RR-SC MCHS

This experimental analysis has clearly shown the trend of the Nu_{ave} ($r = 0.98$) and f_{app} ($r = -0.95$). The Nu_{ave} increased with the increasing of Re, while f_{app} decreased with the increasing of Re. These trends are similar to the simulation results of Nu_{ave} and f_{app}. The simulation and experimental results were compared at the identical condition of Re in order to measure the result deviation between these two nature of works. The details of this analysis is discussed in the next section.

3.3 Validation of TC-RR-SC MCHS Simulation Model

In this section, the simulation and experimental results of Nu_{ave} and f_{app} have been compared for the validation purpose. Figure 19 shows the validation of Nu_{ave} result for the Re of 100 to 500. Both simulation and experimental data had similar trend of the Nu_{ave} augmentation. The maximum discrepancy between both simulation and experimental results was 15.8%. There are few factors that could contribute to the discrepancy of the data. The fabricated TC-RR-SC MCHS have burrs and debris at the top and bottom surface of microchannels. It affected the Nu_{ave} result as the heat transfer coefficient, h increased attributed to the increasing of the heat transfer area provided by the surface area of burrs and debris. Besides that, the fabricated TC-RR-SC MCHS and simulated TC-RR-SC MCHS were different in their number of microchannels. The fabricated TC-RR-SC MCHS have 49 microchannels, while the simulated TC-RR-SC MCHS only have a single microchannel (Single-wall-symmetrical-channel MCHS). Besides the geometry condition of the fabricated TC-RR-SC MCHS, other factors such as unavoidable heat losses from the fitting connections of piping and thermocouple probes also could contribute the data discrepancy.
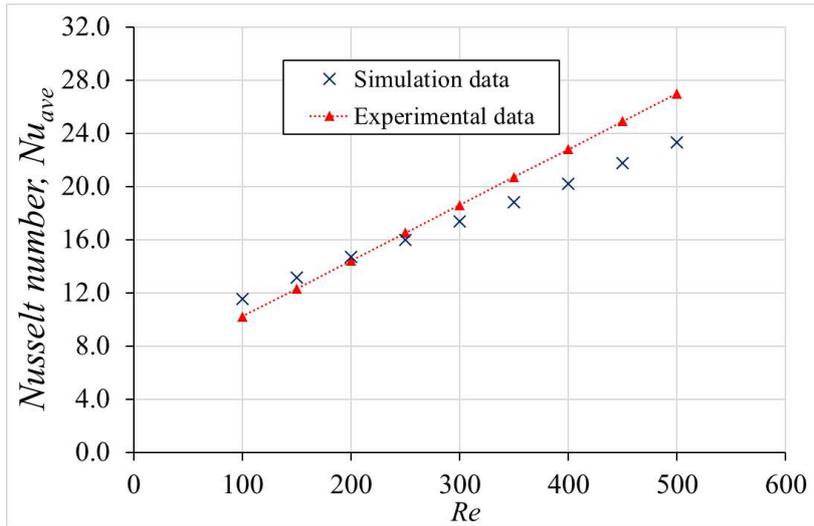
Fig. 19. Validation of the numerical result of Nusselt number, Nu_{ave} with experimental result

Hydrodynamic performance such as friction factor, f_{app} was also validated experimentally for the Re of 100 to 500. As seen in Figure 20, both simulation and experimental data had a similar trend of f_{app}, whereby the f_{app} decreased with the increasing of Re. The validation result illustrated that the maximum discrepancy between both simulation and experimental data was 17.4%. The main reason of the result deviations is that the pressure transducer was not connected directly to the inlet and outlet of the block of the fabricated TC-RR-SC MCHS. This is because the width of the pressure transducer is wider than the length of the block of the fabricated TC-RR-SC MCHS. Therefore, the pressure transducer need to be connected separately from the inlet and outlet of the fabricated TC-RR-SC MCHS. This limitation had contributed to the discrepancy of the data. Besides affected the Nu_{ave} results, the burrs and debris at the top and bottom surface of microchannels also had affected the f_{app} as the pressure drop increased attributed to the decreasing of microchannels flow area. Furthermore, the different number of microchannels between the simulated TC-RR-SC MCHS and fabricated TC-RR-SC MCHS also had contributed to the increasing of data deviation.
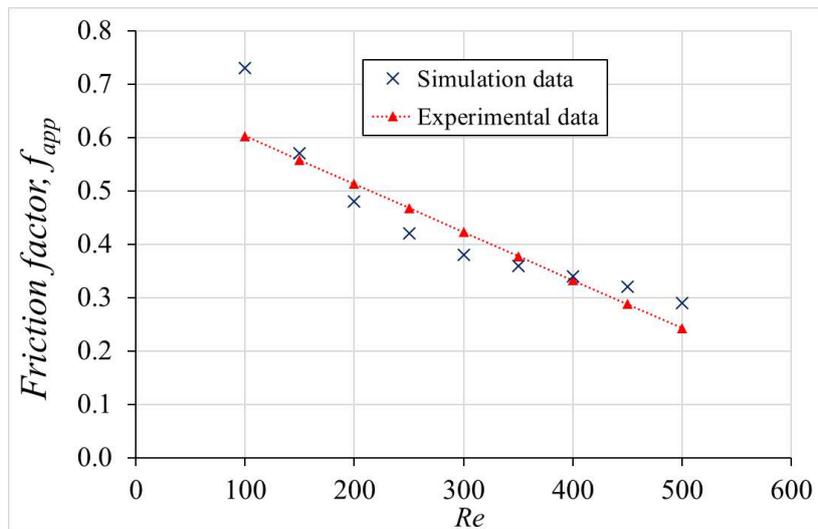

Fig. 20. Validation of the numerical result of friction factor, f_{app} with experimental result

As overall, this analysis showed that the burrs and debris at the top and bottom surface of microchannels, and the number of microchannels affected both Nu_{ave} and f_{app}. To overcome these issues, a harder material than aluminium should be used in the fabrication of TC-RR-SC MCHS so that the inspection, deburring and finishing process can be continued until the end of the fabrication process. Besides that, a computer with higher RAM and uses parallel computing system is required to simulate TC-RR-SC MCHS with 49 microchannles. This is because the generation of meshing process for the TC-RR-SC MCHS with 49 microchannels requires multiple computer cores to run the process simultaneously. Single core with higher RAM is inadequate to generate higher number of element for the mesh generation.

3.4 Temperature Distribution in Conventional MCHS (CR MCHS) and Hybrid MCHS (TC-RR-SC MCHS)

Temperature distribution at the sidewalls of CR MCHS and TC-RR-SC MCHS is illustrated in Figure 21. As seen in the Figure 21(a), CR MCHS exhibited a higher sidewalls temperature distribution than TC-RR-SC MCHS. The reason is that the degrees of fluid mixing in the CR MCHS was lower than TC-RR-SC MCHS. For instance, at $x = 5.8\,mm$, CR MCHS demonstrated that fluid at the central portion of microchannels was cooler than at the sidewalls. Consequently, the generated heat flux could not be removed efficiently as a higher mass flow rate was required in order to continuously replace the hot fluid at sidewalls with the cold fluid. Therefore, a higher pumping power and coolant consumptions were needed in CR MCHS in order to achieve lower temperature distribution in its channels. At $x = 5.8\,mm$, TC-RR-SC MCHS achieved the lowest temperature distribution at the sidewalls. It can be seen that the existence of the rib geometries in TC-RR-SC MCHS reduced the thermal boundary layer as the temperature distribution in the fluid region of TC-RR-SC MCHS was more uniform than in the CR MCHS. Doubtless, the rib geometries significantly improved the heat transfer performance by redeveloping the boundary layer thickness in the TC-RR-SC MCHS which in turn reduced the thermal resistance in its microchannels.
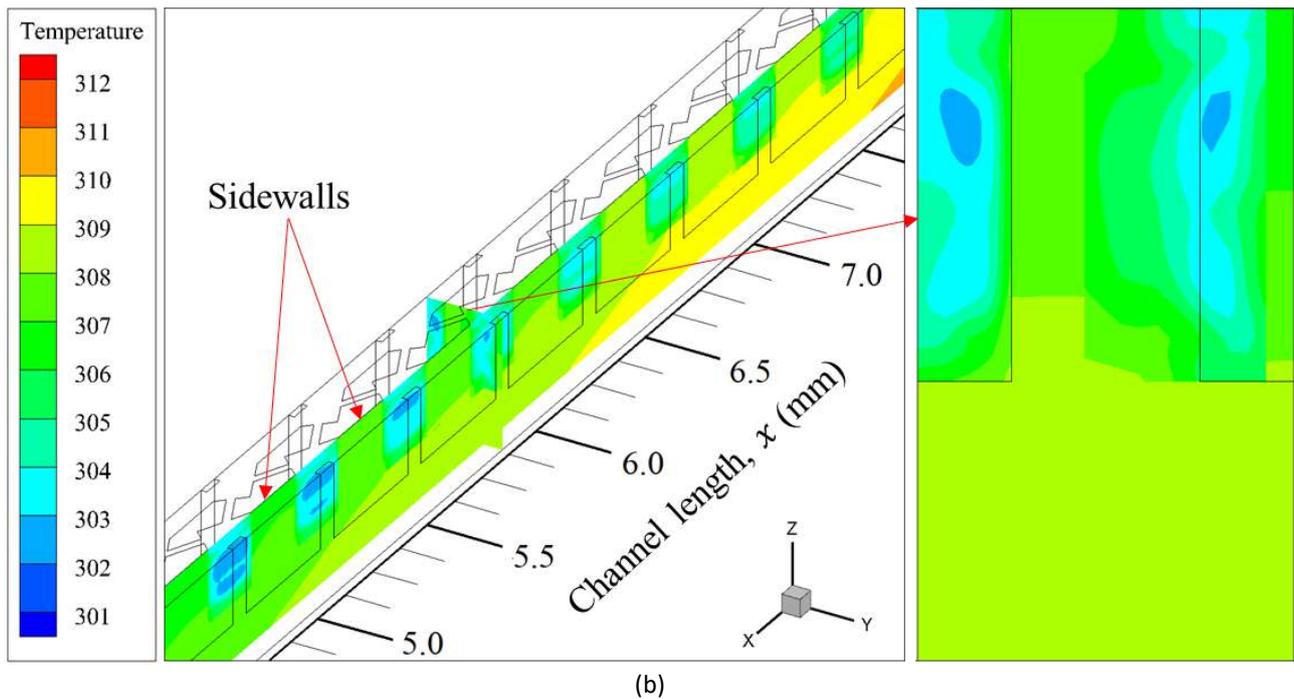

(a)

(b)
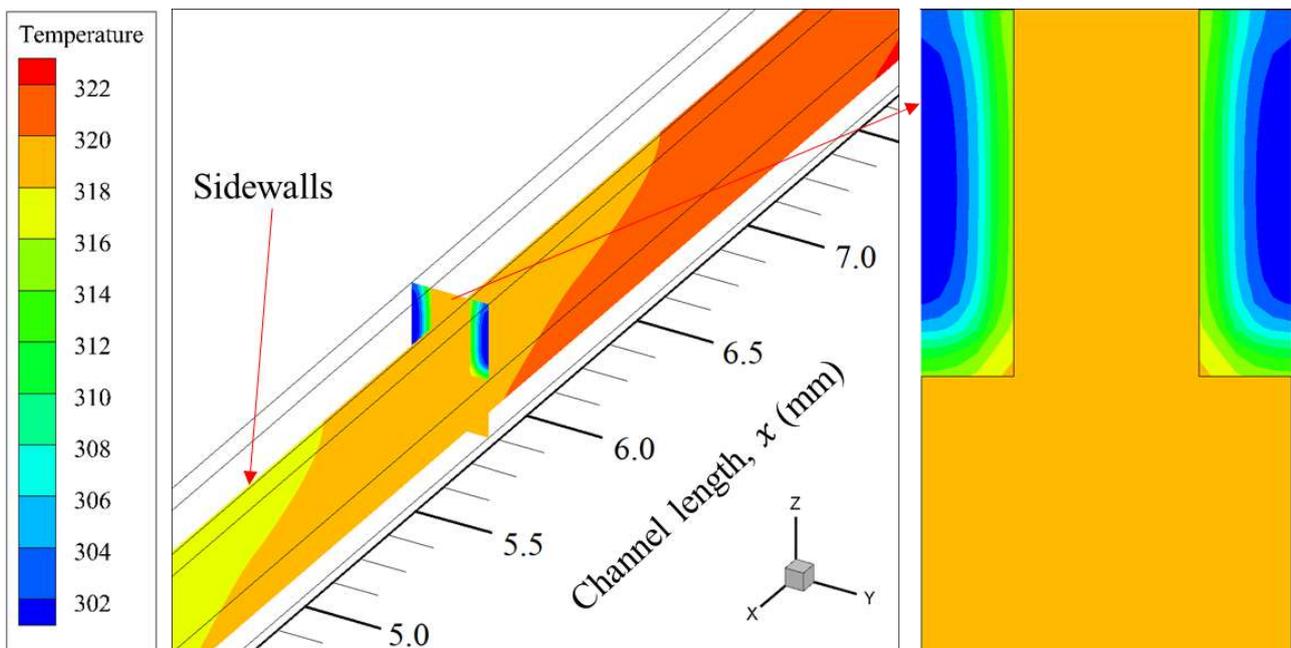
Fig. 21. Temperature distribution (K) at the sidewalls of (a) CR MCHS and (b) TC-RR-SC MCHS at Re=450

Furthermore, the existence of the SC geometries in the TC-RR-SC MCHS increased the degree of fluid mixing between the adjacent channels as illustrated in Figure 21(b). Unlike to the CR MCHS, the temperature distribution of the fluid region in the two adjacent channels of the TC-RR-SC MCHS was the most uniform compared to the CR MCHS. The reason is that, the hot fluid from the sidewalls of a channel flowed through the SC geometries and mixed with the cold fluid, which from the central portion of microchannel, in its adjacent channel. It indicated that the whole fluid region involved with the heat transfer process and carried heat away from the microchannels. Therefore, less pumping power and coolant consumptions are required in order to achieve the optimum heat transfer performance of TC-RR-SC MCHS.

4. Conclusion

The regression analysis of Nu_{ave} has illustrated that, 95% of the variability in Nu_{ave} is explained by the variability in Re (R^2 = 0.9514) while the regression analysis of f_{app} has demonstrated that, 90% of the variability in f_{app} is explained by the variability in Re (R^2 = 0.9037). The validation result showed that the maximum discrepancy between both simulation and experimental analyses for Nusselt number and friction factor were 15.8% and 17.4%, respectively, which is less than 20%. The different number of microchannels between the simulated TC-RR-SC MCHS and fabricated TC-RR-SC MCHS is one of the factors that contribute to the data discrepancy. Furthermore, the poor finishing during the fabrication process also another factor because the burrs and debris at the top and bottom surface of microchannels affect the convective heat transfer area and the flow area of fluid.

It can be seen that TC-RR-SC MCHS can provide sustainable cooling solutions. Thus, this hybrid MCHS is suitable for compact electronic devices that do not require high energy and coolant consumptions for their cooling system. This hybrid MCHS is potentially explored for the usage of other electronic devices and applications.

Acknowledgement

References

[1] Nor Azwadi Che Sidik, Muhammad Noor Afiq Witri Muhamad, Wan Mohd Arif Aziz Japar, and Zainudin A Rasid. "An overview of passive techniques for heat transfer augmentation in microchannel heat sink." *International Communications in Heat and Mass Transfer* 88 (2017): 74-83. https://doi.org/10.1016/j.icheatmasstransfer.2017.08.009

[2] James R Black. "Electromigration—A brief survey and some recent results." *IEEE Transactions on Electron Devices* 16, no. 4 (1969): 338-347. https://doi.org/10.1109/T-ED.1969.16754

[3] E Farsad, SP Abbasi, MS Zabihi, and J Sabbaghzadeh. "Numerical simulation of heat transfer in a micro channel heat sinks using nanofluids." *Heat and mass transfer* 47, no. 4 (2011): 479-490. https://doi.org/10.1007/s00231-010-0735-y

[4] Ihsan Ali Ghani, Nor Azwadi Che Sidik, and Natrah Kamaruzaman. "Hydrothermal performance of microchannel heat sink: The effect of channel design." *International Journal of Heat and Mass Transfer* 107 (2017): 21-44. https://doi.org/10.1016/j.ijheatmasstransfer.2016.11.031

[5] John Francis DuganScott David Anderson, *Electronic device fan mounting system*. 2001, Google Patents.

[6] Yu-Wei Chang, Chiao-Hung Cheng, Jung-Chang Wang, and Sih-Li Chen. "Heat pipe for cooling of electronic equipment." *Energy conversion and management* 49, no. 11 (2008): 3398-3404. https://doi.org/10.1016/j.enconman.2008.05.002

[7] Yueguang DengJing Liu. "A liquid metal cooling system for the thermal management of high power LEDs." *International Communications in Heat and Mass Transfer* 37, no. 7 (2010): 788-791. https://doi.org/10.1016/j.icheatmasstransfer.2010.04.011

[8] Liang Gong, Jin Zhao, and Shanbo Huang. "Numerical study on layout of micro-channel heat sink for thermal management of electronic devices." *Applied Thermal Engineering* 88 (2015): 480-490. https://doi.org/10.1016/j.applthermaleng.2014.09.048

[9] Jung-hyun Lee, *Micro cooling device*. 2004, Google Patents.

[10] Mark E. SteinkeSatish G. Kandlikar. *Single-Phase Heat Transfer Enhancement Techniques in Microchannel and Minichannel Flows*. in *ASME 2004 2nd International Conference on Microchannels and Minichannels*. 2004. https://doi.org/10.1115/ICMM2004-2328

[11] NM Noh, A Fazeli, and NA Che Sidik. "Numerical simulation of nanofluids for cooling efficiency in microchannel heat sink." *Journal of Advanced research in fluid mechanics and thermal sciences* 4, no. 1 (2014): 13-23.

[12] David B TuckermanRoger Fabian W Pease. "High-performance heat sinking for VLSI." *IEEE Electron device letters* 2, no. 5 (1981): 126-129. https://doi.org/10.1109/EDL.1981.25367

[13] Wan Mohd Arif Aziz Japar, Nor Azwadi Che Sidik, Natrah Kamaruzaman, Yutaka Asako, and Nura Mu'az Muhammad. "Hydrothermal performance in the Hydrodynamic Entrance Region of Rectangular Microchannel Heat Sink." *Journal of Advanced Research in Numerical Heat Transfer* 1, no. 1 (2020): 22-31.

[14] Pankaj Srivastava, Anupam Dewan, and Jugal K Bajpai. "Flow and heat transfer characteristics in convergent-divergent shaped microchannel with ribs and cavities." *International Journal of Heat and Technology* 35, no. 4 (2017): 863-873. https://doi.org/10.18280/ijht.350423

[15] YF Li, GD Xia, DD Ma, YT Jia, and J Wang. "Characteristics of laminar flow and heat transfer in microchannel heat sink with triangular cavities and rectangular ribs." *International Journal of Heat and Mass Transfer* 98 (2016): 17-28. https://doi.org/10.1016/j.ijheatmasstransfer.2016.03.022

[16] Yifan Li, Guodong Xia, Yuting Jia, Dandan Ma, Bo Cai, and Jun Wang. "Effect of geometric configuration on the laminar flow and heat transfer in microchannel heat sinks with cavities and fins." *Numerical Heat Transfer, Part A: Applications* 71, no. 5 (2017): 528-546. https://doi.org/10.1080/10407782.2016.1277940

[17] Ihsan Ali Ghani, Natrah Kamaruzaman, and Nor Azwadi Che Sidik. "Heat transfer augmentation in a microchannel heat sink with sinusoidal cavities and rectangular ribs." *International Journal of Heat and Mass Transfer* 108 (2017): 1969-1981. https://doi.org/10.1016/j.ijheatmasstransfer.2017.01.046

[18] GuoDong Xia, YuLing Zhai, and ZhenZhen Cui. "Characteristics of entropy generation and heat transfer in a microchannel with fan-shaped reentrant cavities and internal ribs." *Science China Technological Sciences* 56, no. 7 (2013): 1629-1635. https://doi.org/10.1007/s11431-013-5244-z

[19] GD Xia, YT Jia, YF Li, DD Ma, and B Cai. "Numerical simulation and multiobjective optimization of a microchannel heat sink with arc-shaped grooves and ribs." *Numerical Heat Transfer, Part A: Applications* 70, no. 9 (2016): 1041-1055. https://doi.org/10.1080/10407782.2016.1230394

[20] Yonghui Xie, Zhongyang Shen, Di Zhang, and Jibing Lan. "Thermal performance of a water-cooled microchannel heat sink with grooves and obstacles." *Journal of Electronic Packaging* 136, no. 2 (2014): https://doi.org/10.1115/1.4025757

[21] Nor Haziq Naqiuddin, Lip Huat Saw, Ming Chian Yew, Farazila Yusof, Hiew Mun Poon, Zuansi Cai, and Hui San Thiam. "Numerical investigation for optimizing segmented micro-channel heat sink by Taguchi-Grey method." *Applied Energy* 222 (2018): 437-450. https://doi.org/10.1016/j.apenergy.2018.03.186

[22] ANSYS. *ANSYS 17.0*. 2016; Available from: https://www.ansys.com/.

[23] Wan Mohd Arif Aziz Japar, Nor Azwadi Che Sidik, and Shabudin Mat. "A comprehensive study on heat transfer enhancement in microchannel heat sink with secondary channel." *International Communications in Heat and Mass Transfer* 99 (2018): 62-81. https://doi.org/10.1016/j.icheatmasstransfer.2018.10.005

[24] Ahmad Reza Rahmati, Omid Ali Akbari, Ali Marzban, Davood Toghraie, Reza Karimi, and Farzad Pourfattah. "Simultaneous investigations the effects of non-Newtonian nanofluid flow in different volume fractions of solid nanoparticles with slip and no-slip boundary conditions." *Thermal Science and Engineering Progress* 5 (2018): 263-277.

[25] Abdullah AAA Alrashed, Omid Ali Akbari, Ali Heydari, Davood Toghraie, Majid Zarringhalam, Gholamreza Ahmadi Sheikh Shabani, Ali Reza Seifi, and Marjan Goodarzi. "The numerical modeling of water/FMWCNT nanofluid flow and heat transfer in a backward-facing contracting channel." *Physica B: Condensed Matter* 537 (2018): 176-183.

[26] Y. J. Lee, P. S. Lee, and S. K. Chou. "Enhanced Thermal Transport in Microchannel Using Oblique Fins." *Journal of Heat Transfer* 134, no. 10 (2012): https://doi.org/10.1115/1.4006843

[27] Hassanali Ghaedamini Harouni, *Investigation of chaotic advection regime and its effect on thermal performance of wavy walled microchannels*. 2015.

[28] Warren M Rohsenow, James P Hartnett, and Young I Cho, *Handbook of heat transfer*. Vol. 3. 1998, New York: McGraw-Hill

[29] Hugh W ColemanW Glenn Steele, *Experimentation, validation, and uncertainty analysis for engineers*. 2018: John Wiley & Sons.